Journal of Volcanology and Geothermal Research 468 (2025) 108443

Contents lists available at ScienceDirect

Journal of Volcanology and Geothermal Research

journal homepage: www.journals.elsevier.com/journal-of-volcanology-and-geothermal-research

Insights on the multi-scale topographic features of Mt. Etna volcano (Italy)

Salvatore Scudero [a],*, Gianluca Groppelli [b]

[a] Istituto Nazionale di Geofisica e Vulcanologia, Osservatorio Nazionale Terremoti, Via di Vigna Murata 605, 00143 Rome, Italy
[b] Consiglio Nazionale delle Ricerche - Istituto di Geologia Ambientale e Geoingegneria, sez. di Milano, via M. Bianco 9, 20131 Milan, Italy

ARTICLE INFO

Keywords:
Terrain analysis
Volcano
Wavelet
Morphology
Topography
Etna

ABSTRACT

The terrain analysis of volcanic landforms provides valuable qualitative and quantitative insights into the factors that shape volcanoes. Using different terrain analysis approaches, this study reconstructs and describes the multi-scale topographic features of Mt. Etna Volcano (Italy). Specifically, the first order shape of the volcano, approximating the large-scale volcanic edifice, is characterized through the analytical fitting of contour lines using an elliptical geometry. The geometric properties of this modelled surface align with the evolutionary phases of Mt. Etna over the past 300 kyr. The modelled surface also serves as a two-dimensional filter: the residual topography, obtained by its removal from the actual topography, reveals second-order topographic features. The residual topography is then opportunely resampled and analysed using the wavelet technique along slope-parallel and base-parallel sections. This analysis reveals zones with different wavelength behaviours that correlate with the residual topographic anomalies. The spatial arrangement of this anomalies around the flanks of the volcano aligns with known volcanic features of Mt. Etna, such as the "Ellittico" volcano and its caldera depression, the large volcano-tectonic depression of the "Bove" valley, and the unstable eastern flank. A few zones do not correspond to any recognized features and may suggest the occurrence of buried structures, offering potential targets for future investigation. This study demonstrates that the wavelet-based technique is a valuable tool for characterizing and classifying volcanic landforms.

1. Introduction

The study of volcano morphology serves several purposes, including the classifications of landforms, understanding formation mechanisms, and quantitatively estimating process rates (Thouret, 1999). Actually, the factors controlling volcano morphology involve a range of volcanological and geological processes, such as magma output rate, hiatus in volcanic activity, edifice strength and erosion rate, volcano-tectonic processes, and even the climate influence. Given this wide range of potential controlling factors, the quantitative analysis of volcanic morphologies has been a highly relevant topic in the last decades, and interest in this field is expected to grow further, driven by the increasing availability of data (Carrión-Mero et al., 2020). Research on volcanic landforms spans various scales, addressing topics from basic classifications of volcanic shapes (Norini et al., 2004; Grosse et al., 2012, 2014; Grosse and Kervyn, 2018), to the development of evolutionary models (Favalli et al., 2005; Grosse et al., 2009), the construction history and growth rate of a volcanic edifice (Székely and Karátson, 2004; Lahitte et al., 2012; Salvany et al., 2012; Kereszturi et al., 2013; Ricci et al., 2015; Karlstrom et al., 2018; Dibacto et al., 2020; O'Hara and Karlstrom, 2023; Gayer et al., 2021), as well as the reconstruction of eroded morphologies (e.g. gullies or flank collapse) and the assessment of erosion rates (Karátson et al., 2012; Bossis et al., 2023; Karátson et al., 2016; O'Hara et al., 2024).

Within this wide broad scope of studies,elevation data represent the core information for terrain analysis. The availability and reliability of elevation data have significantly improved in recent years, thanks to the development of various surveying techniques (Gomez, 2022; Wilson, 2022). The vast quantity and high quality of these data, combined with the enhanced computational capabilities, have enabled the application of numerous data processing techniques (Franklin, 2020; Xiong et al., 2022). Among the various methods for terrain analysis, spectral techniques are widely employed due to their unique characteristics, particularly their ability to discriminate among different signal sources, enhance features that would otherwise remain hidden, and perform applications across different scales. Examples of the application of spectral techniques to terrain analysis are well documented in the literature (Jordan and Schott, 2005; Lashermes et al., 2007; Perron et al., 2008; Struble et al., 2021; Struble and Roering, 2021; Maxwell and Shobe, 2022; Xu et al., 2021), and they have also been used in the study of different volcanic features (Tort and Finizola, 2005; Lescinsky et al., 2007; Zarazúa-Carbajal and De la Cruz-Reyna, 2020); Spectral

* Corresponding author.
E-mail address: salvatore.scudero@ingv.it (S. Scudero).

https://doi.org/10.1016/j.jvolgeores.2025.108443
Received 25 June 2025; Received in revised form 10 September 2025; Accepted 12 September 2025
Available online 19 September 2025
0377-0273/© 2025 The Authors. Published by Elsevier B.V. This is an open access article under the CC BY-NC-ND license (http://creativecommons.org/licenses/by-nc-nd/4.0/).

techniques help in the detection and characterization of morphological features that might otherwise be concealed or overlapped. Among these spectral methods, we employed the wavelet analysis, which is likely the most widely adopted due to its flexibility and high spatial and frequency resolution. Wavelet decomposition was originally developed for signal analysis, but due to its characteristics, it is widely employed to study the topographic relief, including volcanic landforms, at different spatial scales (Little et al., 1993; Guillou-Frottier et al., 2007; Chamoli, 2009; Cadio et al., 2012; Kalbermatten et al., 2012; Gomez, 2012, 2018; Struble and Roering, 2021; Struble et al., 2021; Xu et al., 2021).

A quantitative description of the general morphology of Mt. Etna volcano (Italy) was first proposed by Favalli et al. (1999). Detailed terrain analyses, also using spectral techniques, have been primarily focused on small-scale features like scoria cones (Favalli et al., 2009) and individual lava flows (Tarquini et al., 2012; Favalli et al., 2018). However, a recent, comprehensive, and multi-scale investigation of the entire volcano is lacking. This study aims at analysing the first- and second-order morphological features of Mt. Etna. After constructing a model of the volcano's surface, the residual topography is examined using the wavelet technique to correlate the morphological features with the various processes that contributed to shaping Mt. Etna. The volcano's complex evolution has led to its present-day composite morphology, involving the complex interaction among constructive and destructive phases, tectonics, feeding systems displacement, and magmatic and volcano-tectonic processes; this study offers insights into these relationships.

2. Case study: Etna volcano

Mount Etna volcano is located in the eastern part of Sicily (Italy), at the intersection of several major regional tectonic lineaments, where many tectonic blocks interact (Catalano et al., 2008; Monaco et al., 1997; Barreca et al., 2018b; Gambino et al., 2022) (Fig. 1a). Etna's evolution has gone through various phases: the earliest volcanic products are dated to approximately ~ 500 ka (Branca et al., 2008), while the two main phases leading to the formation of the volcanic edifice began at around 110 and 60 ka, respectively (De Beni et al., 2011). These phases, up to the most recent one starting at 15 ka, are distinguished based on major stratigraphic unconformities. Each phase is marked by differences in magma composition, eruptive style, and magma production rate (Branca et al., 2011a,b). The origin of Etna, along with its subsequent stages of evolution, was controlled by regional geodynamic processes occurring in the area, such as rollback and detachment of the Ionian slab, mantle flow, and crustal collision. However, there is no single interpretation of these events (Gvirtzman and Nur, 1999; Doglioni et al., 2001; Schellart, 2010; Faccenna et al., 2011; Barreca et al., 2018a; Firetto Carlino et al., 2019; Barreca et al., 2020). The complex interaction between multiple processes operating at different scales, and even their potential role on the future evolution of the volcanism, has been suggested by several studies (Monaco et al., 1997; De Guidi et al., 2013; Scudero et al., 2019; Barreca et al., 2020; Scudero, 2024).

From a morphological perspective, the volcanic edifice of Mt. Etna today reaches an elevation of ~ 3400 m a.s.l. De Beni et al. (2025). The volcanic products piled over a sedimentary substratum characterized by an articulated topography (Branca and Ferrara, 2013), which experienced vertical uplift during the late Pleistocene at rates between 0.5 and 1.7 mm/yr (Di Stefano and Branca, 2002; De Guidi et al., 2012, 2014; Scudero et al., 2015). The shape of the upper portion of the volcano edifice (above ~ 1000 m a.s.l) can be fairly approximated by a symmetric cone. The lower part of the edifice has a gentler slope and can be approximated by a slightly asymmetric ellipsoid. It is bordered by the surrounding reliefs of the Apennine chain on the northern, western, and part of the southern flanks, while the remaining southern and eastern flanks have lower topography, allowing the volcanic deposits to spread in these directions towards the coast (Fig. 1b). According to the most recent estimates by Barreca et al. (2018a), the total volume of volcanic material accumulated over time at Etna is 535 ± 59 km^3.

The main morphological feature of the volcanic edifice is interpreted as a tectonic depression known as "Valle del Bove" measuring 6.5 by 5 km, which significantly impacts the eastern flank (Fig. 1b). It is interpreted as the results of one, or more, lateral collapses generating debris avalanches, linked to the interplay between morphological and volcano-tectonic processes. The proposed timing of the formation of the "Valle del Bove" is not univocal: considering all the available age determinations, the initial stage has been dated between 10 and 6.3 kyr and the final stage between 5.3 and 2.0 kyr (Guest et al., 1984; Calvari et al., 1998, 2004; Malaguti et al., 2023). Another important volcano-tectonic feature is represented by the morphology of the Ellittico caldera, mostly covered by Mongibello volcano lava flows, but still preserved in Pizzi Deneri and Punta Lucia localities (Branca et al., 2011a). At a finer scale, the volcanic edifice is affected by a network of active lineaments, which may have a morphological expression depending on their kinematics (Monaco et al., 1997; Favalli et al., 1999). Their role is likely associated both with regional tectonics and the instability of the eastern flank (Palano, 2016; De Guidi et al., 2018; Urlaub et al., 2018). Lastly, numerous monogenetic cones are distributed all around the flanks of Mt. Etna (Fig. 1b). Their heights rarely exceed 100 m, and their maximum diameters range between 700 and 800 m (Favalli et al., 2009).

The present-day morphology of Etna is therefore the result of a combination of construction and dismantling processes. It is of great interest to decompose its topography in order to recognize the signs of the processes involved and their respective roles.

3. Methods

The terrain analysis was performed in several steps: (i) defining a reference surface that approximates the topographic surface, (ii) extracting and preparing the residual elevation data, and, (iii) performing a spectral analysis of the topographic relief using the wavelet decomposition technique. The data used for this work come from a digital elevation model (DEM) with a 2 m pixel resolution and 0.3 m accuracy derived from the processing of LIDAR acquisitions (Regione Siciliana, 2013).

Although many large volcanic edifices develop over long time spans, composite volcanoes often exhibit a first-order regular and axisymmetric trend in their flanks (de Silva and Lindsay, 2015). As a result, the shape of many volcanoes can be well approximated by "ideal" shapes (Karátson et al., 2010a; Davidson et al., 2000), that can be simply described in analytical form (Karátson et al., 2012; Favalli et al., 2014; Cosburn and Roy, 2020). It is widely recognized that such "fitted shapes" provide valuable insights into the processes that led to the construction of volcanic edifices, help reconstruct ancient morphologies by evaluating deviations from these regular trends, and allow for the assessment of long-term erosion rates (Karátson et al., 2010b, 2012; Ricci et al., 2015; Karátson et al., 2016; Gayer et al., 2021; Bossis et al., 2023) The simplest of these geometries is an axisymmetric shape, which can be easily determined by interpolating the radial profile obtained by plotting the elevation of each surface unit against its distance from the volcano center.

However, the edifice of Mt. Etna cannot be approximated as a circular, axisymmetric shape because of its composite evolution, which involved the movements of the feeding system over time and the transition from a shield volcano to a stratovolcano (Branca et al., 2011a). Instead, the slopes of Etna can be more accurately approximated by an elliptical base rather than a circular one. Elliptical symmetry describes the shape of many other volcanoes worldwide (Favalli et al., 2014; Cosburn and Roy, 2020). To reconstruct a reference surface, the elevation data sampled at regular intervals were fitted with regular ellipses by means of a least-squares approach. This method minimizes the geometric distance from the observed points to the fitting curve (Chernov

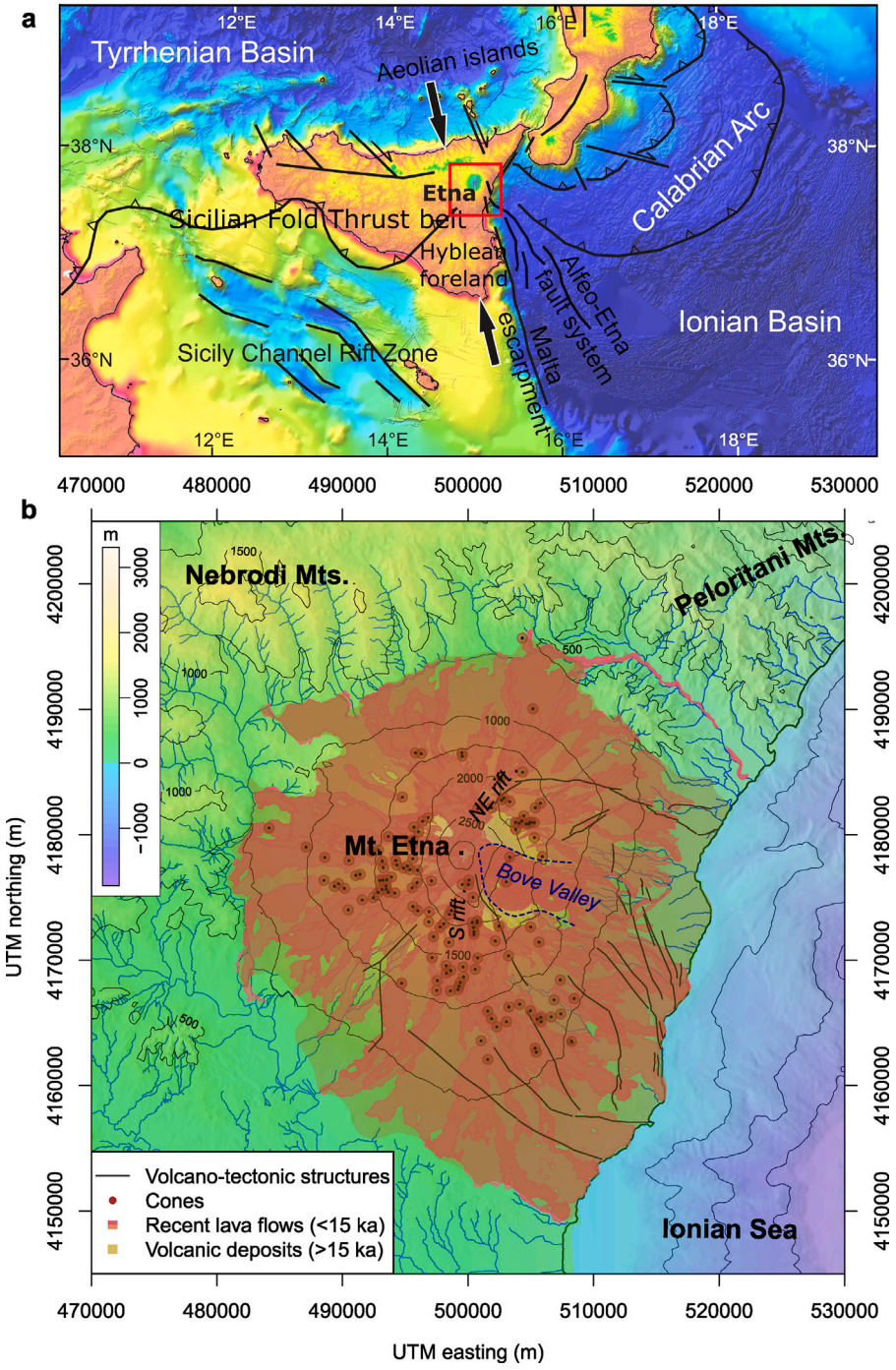

Fig. 1. (a) Geodynamic setting of the central Mediterranean area and location of the study area (red rectangle); main lineaments are drawn from Catalano et al. (2008), Del Ben et al. (2008), Polonia et al. (2011), and Gambino et al. (2022). The paired arrows represent the orientation of the main tectonic stress acting in the area. (b) Map showing the main morphological and geological features in the area of Mt. Etna volcano; lineaments are drawn from Barreca et al. (2013), cones from Favalli et al. (2009).

et al., 2014). The equation of an ellipse centred at (x_c, y_c) is given by the formula: $(x - x_c)^2/a^2 + (y - y_c)^2/b^2 = 1$; where a and b are the lengths of the major and minor semi-axes, respectively. Thus, an ellipse is described by a set of five parameters: the coordinates of the center, the lengths of the axes, and the angle of rotation. To further characterize the fitted ellipses, the eccentricity e is calculated, defined as: $e = \sqrt{1 - (b^2/a^2)}$ with $0 \leq e < 1$, where $e = 0$ corresponds to a perfect circle, and increasing values indicate progressively more elongated ellipses.

For the application to Mt. Etna, the ellipses were fitted in the elevation range of 500 to 3200 m a.s.l. with a constant interval of 20 m. A total of 136 ellipses were generated and subsequently interpolated together to model a reference surface for the volcanic edifice. In particular, kriging interpolation was performed by modelling the omnidirectional semi-variograms to infer the interpolation parameters (nugget, sill, and range). Kriging was selected over other methods because it provides an estimation of the interpolation error. The interpolation was performed over a grid with resolution of 0.25 × 0.25

km, covering an area of 36 × 41 km. The outer portions of the model, where the predicted standard error is higher, were removed from the final surface.

The fitted surface was used to map and quantify the elevation differences relative to the actual topography. Local features such as cones, lava flows, ridges, landslides, valleys, and erosional landforms in general, introduce "noise" into the ellipse fitting procedure. While very small-scale features are smoothed out, larger ones remain identifiable and are enhanced. The aim of this study is to analyse these features, which represent the second-order morphological characteristics of Etna's volcanic edifice, revealed after filtering out the first-order shape.

The methodology proposed to detect and characterize second-order features is the wavelet methodology, which holds advantages over other spectral techniques. For instance, Fourier analysis provides frequency content averaged over the entire signal, making it unable to resolve local variations in temporal (or spatial) frequency. Even when applied to windowed signals, the resulting temporal (or spatial) resolution is coarser compared to the wavelet method (Little et al., 1993). Wavelet analysis, on the other hand, allows for finer spectral coverage, enabling simultaneous localization in both the spatial and frequency domains, thus resolving variations across multiple scales. This makes it particularly suitable for complex, non-stationary signals and can help highlight subtle morphological features that might otherwise be overlooked (Little et al., 1993; Kalbermatten et al., 2012).

In general terms, a Wavelet Transform (WT) decomposes a signal into a set of basic functions, which are expansions, contractions, and translations of a function called the "mother wavelet" $\psi(t)$ (Daubechies, 1992). Considering the space $L^2(R)$ as the set of square integrable functions satisfying $\int_{-\infty}^{+\infty}|g(t)|^2dt<\infty$, and using the capital letter, G(t) to represent the Fourier transformation of a given function, $G(\omega)=\int_{-\infty}^{+\infty}g(t)e^{(-i\omega t)}dt$. A function $\psi(t)\in L^2(R)$ that satisfies the admissibility condition $\Psi(0)=\int_{-\infty}^{+\infty}\psi(t)dt=0$ is the called "mother wavelet". A double-indexed family of "wavelet daughters" is obtained by shifting and scaling the mother function $\psi(\cdot)$: $\psi_{\tau,s}(t)=|s|^{-1/2}\psi\left(\frac{t-\tau}{s}\right)$ with $s,\tau\in R$ and $s\neq 0$.

For the purpose of this research, the well-known, flexible, and complex-valued Morlet mother wavelet has been adopted (Grossmann and Morlet, 1984). It is expressed as: $\psi(t)=\pi^{-1/4}e^{i\omega t}e^{-t^2/2}$. Different types of wavelets have been proposed for the study of topographic relief (Guillou-Frottier et al., 2007; Doglioni and Simeone, 2014); however, the Morlet wavelet provides a good balance between time (i.e space) and frequency (i.e. wavelength) localization because it is characterized by a rapid decay in both domains (Little et al., 1993).

The local Wavelet Power Spectrum (WPS) based on the CWT of a given function $g(t)\in L^2(R)$ with respect to the wavelet family is:

$$|WPS|_g(\tau,s)=|W_{x;\psi}(\tau,s)|^2=\left|\int_{-\infty}^{+\infty}g(t)|s|^{-1/2}\psi^*\left(\frac{t-\tau}{s}\right)dt\right|^2 \quad (1)$$

where * indicates the complex conjugate operation, s is the dilation (scale) parameter controlling the width of the wavelet, which is inversely proportional to the frequency, while τ defines the shifting (translation) in the spatial domain. The WPS (Eq. (1)) can be interpreted as the local variance of the analysed signal.

This quantity can be averaged over the spatial coordinate (τ) to obtain what is called the global WPS,

$$\int_{-\infty}^{+\infty}|W_{x;\psi}(\tau,s)|^2d\tau \quad (2)$$

Therefore, local maxima in the global WPS curve indicate the main wavelengths present in the signal.

The wavelet technique requires regular time (spatial in this case) series. To meet this requirement, the DEM was sampled at a regular distance along two sets of cross-sections: slope-parallel (i.e. radial) and base-parallel. Given the a roughly conical shape of Mt. Etna, this sampling strategy enables the reconstruction of the 2D spatial pattern using a 1D analysis method, rather than a classical Cartesian coordinate system. Radial profiles were systematically drawn at 2° interval obtaining 180 traces, which were later paired to obtain 90 cross sections spanning across the volcano. Diameter, rather than radius, sections are considered because edge effects would have affected the central part (i.e. the summit) and also narrowed the upper limit of the analysed bandwidth. In fact, the longer the series, the more reliable are the results of the spectral analysis; as a general rule, the maximum wavelength that can be reliably detectable is equal to one-third of the series length. The considered wavelength interval ranges from 0.125 to 16 km.

Base-parallel sections follow the contours of five fitted ellipses, as previously described, located at elevations ranging from 1000 to 3000 m a.s.l., with intervals of 500 m. Each of these five base-parallel traces was sampled at regular intervals, resulting in a greater number of samples for the outer ellipses. Alternatively, a fixed number of samples with varying sampling frequencies could have been used, allowing for easier comparison between sections (Gomez, 2012). However, the former option was preferred to avoid potential issues in the spectral analysis. Finally, the wavelet power spectra, calculated for signals of different length, were appropriately stretched to ensure alignment across all sections.

The coordinates of the points sampled along all the slope-parallel sections were transformed from the geographic projection system of the DEM into a polar coordinate system, and subsequently into series suitable for spectral analysis. The origin of the polar system $O_{(x_0,y_0)}$ is the centre of the highest fitted ellipse at an elevation of 3200 m a.s.l., located at 37.752 ^oN, 14.995 ^oE. Each sampled point $P_{(x,y)}$ is expressed in terms of radial distance $r=\sqrt{(x-x_0)^2+(y-y_0)^2}$ and azimuth $\phi=arctan((y-y_o)/(x-x_0))$ or $\phi=0$ when $x=x_0$ (i.e. north direction).

Then the elevation series z consist of points with equal azimuth ϕ for the slope-parallel profiles (cross-sections), or points with equal fitted elevation for the base-parallel sections. In both cases, the spacing between two consecutive points is constant and fixed at $a=5$ m. For the base-parallel sections, the number of samples increases progressively from 1381 up to 14,517 from the innermost to the outermost ellipse, respectively.

The analyses were performed using the *WaveletComp* package (Roesch et al., 2014) in the *R* statistical software (R Development Core Team, 2005).

4. Results

4.1. Surface modelling

As introduced in the previous section, modelling Etna's surface was a preliminary step aimed at filtering out the volcano's first-order morphology from the topographic data. The model was obtained from the interpolation of the fitted ellipses within the elevation range of 500–3200 m a.s.l. The parameters describing the set of fitted ellipses are presented in Fig. 2. As elevation increases, the centre of the fitted ellipses shifts approximately 2 km from West to East (from ~ 500 to ~ 2000 m a.s.l.), then moves southwards by about 500 m (up to 2600 m a.s.l.), and finally westwards by about 500 m, converging near the position of the present-day summit (Fig. 2b). The eccentricity values (Fig. 2c) exhibit some variability up to ~ 1200 m a.s.l., after which a steady increase is observed, reaching a maximum value of 0.81 at about 2100 m a.s.l. Above the elevation of about 2400 m a.s.l., the eccentricity decreases reaching a local minimum at around 3000 m of elevation. Overall, the eccentricity is relatively low, indicating that most of fitted ellipses approximate circles. However, the ellipses become more flattened in the elevation interval from 1800 to 2600 m a.s.l., where the major axis exceeding 1.5 times the length of the minor axis. The rotation angle of the major axis shows significant variability when the circularity is lower, whereas it shows an almost constant

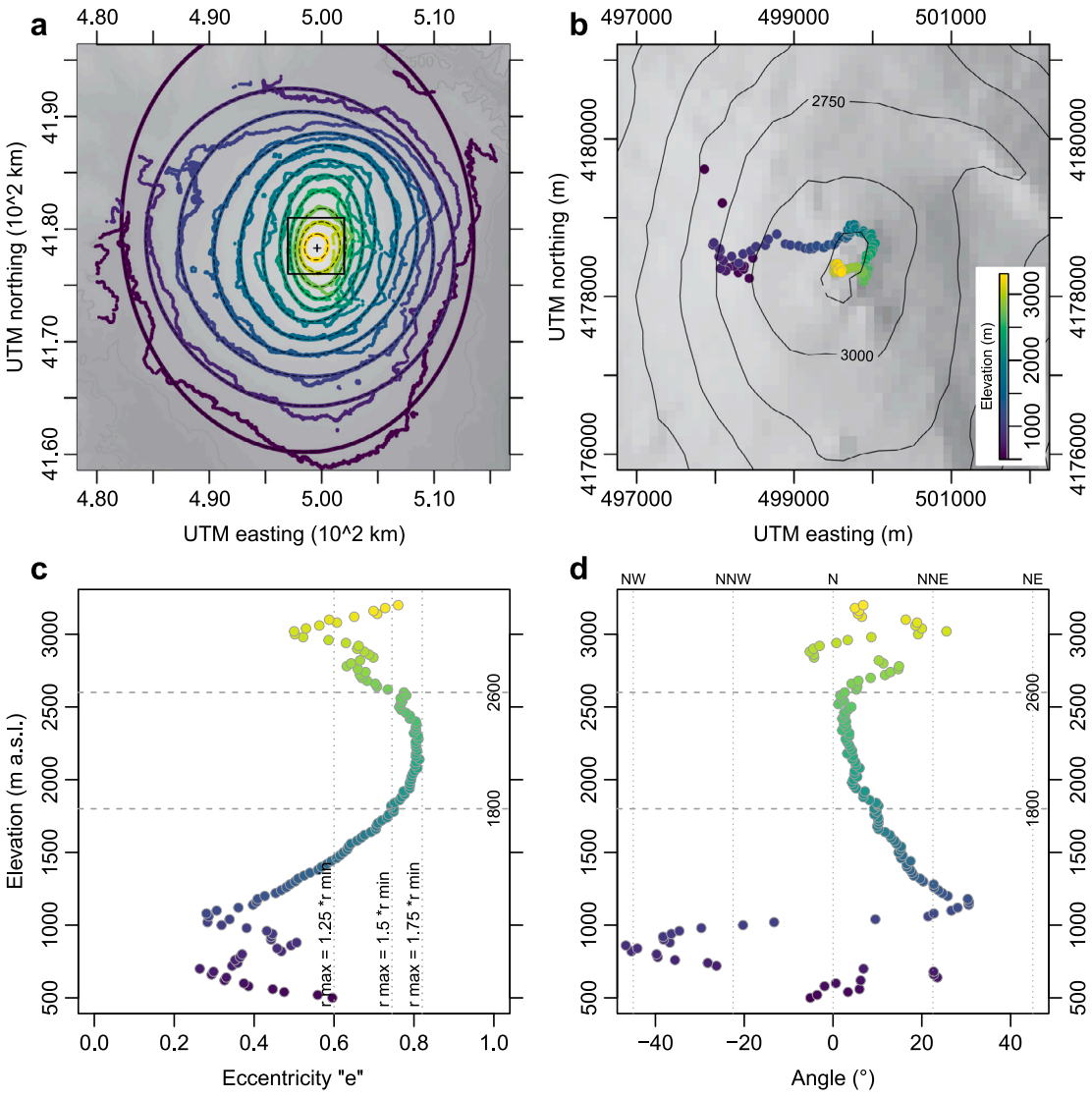

Fig. 2. (a) Examples of contour lines fitting with regular ellipses at elevation interval of 250 m; the grey rectangle indicates the extension of the panel "b". (b) Locations of the centres of the fitted ellipses at altitude from 500 m to 3200 m and elevation intervals of 20 m. (c) Eccentricity values plotted against elevation; the eccentricity e is calculated for the ellipses fitting contour lines from 500 to 3200 m at elevation intervals of 20 m. The elevation limits of the region with the relatively higher eccentricity values ($e > 0.75$) are 1800 and 2600 m a.s.l. corresponding to a ring region located approximately between 2.5, and 6 km away from the centre of the volcano. (d) Angle of the major axis of the fitted ellipse with respect to the North direction calculated at elevation intervals of 20 m.

counterclockwise trend in the elevation range from 1200 m to 2600 m a.s.l., shifting from a NNE to a *N* orientation (Fig. 2a,d).

The fitted ellipses were spatially interpolated to obtain a model representing the first-order shape of Etna. The error associated with the model remains constant at its lowest values in the central part of the study area (Fig. 3a). The outer region was removed from the final model (Fig. 3b) due to the higher error values. The resulting model resembles a sombrero-like surface (Fig. 3b and 4b), with the slope of the flanks increasing upslope before decreasing approaching the summit.

The difference between the elevation map (DEM) and the modelled topography is shown in Fig. 3c. Residual values generally fall within the interval ±400 m, with most values in the ±150 m range; their frequency distribution is symmetric (Fig. 3c). The residual pattern reveals several distinct features characterized by positive and negative values. Notably, a positive anomaly marks the central portion, surrounded by three localized negative anomalies. A large part of the area is marked by negative residual values, which are more accentuated in the eastern flank (Fig. 3c). Positive residuals mark a small portion of the medium western flank, a sector in the north-eastern flank, and another sector in the southern flank (Fig. 3c). A comparative perspective view of Etna's topography, the fitted reference surface, and the resulting residual topography is presented in Fig. 4.

4.2. Wavelet analysis

The residual topography, obtained from the removal of the first-order shape of the cone, was sampled along both slope-parallel and base-parallel sections. Wavelet analysis was then applied to all these sections. The surface modelling is a necessary preliminary step for wavelet method. In fact, the main limit on the applicability of spectral techniques is that topographic data do not meet the stationarity assumption. Even though wavelet technique (with respect to Fourier Transform) allows for a certain degree of nonstationarity, the first-order volcano morphology represents a signal of great variability. The capability to model it and filtering it out with only the application of the spectral technique, would be extremely low. Therefore, the contour-based interpolation is the most effective and reliable way to obtain the accurate surface modelling and removal.

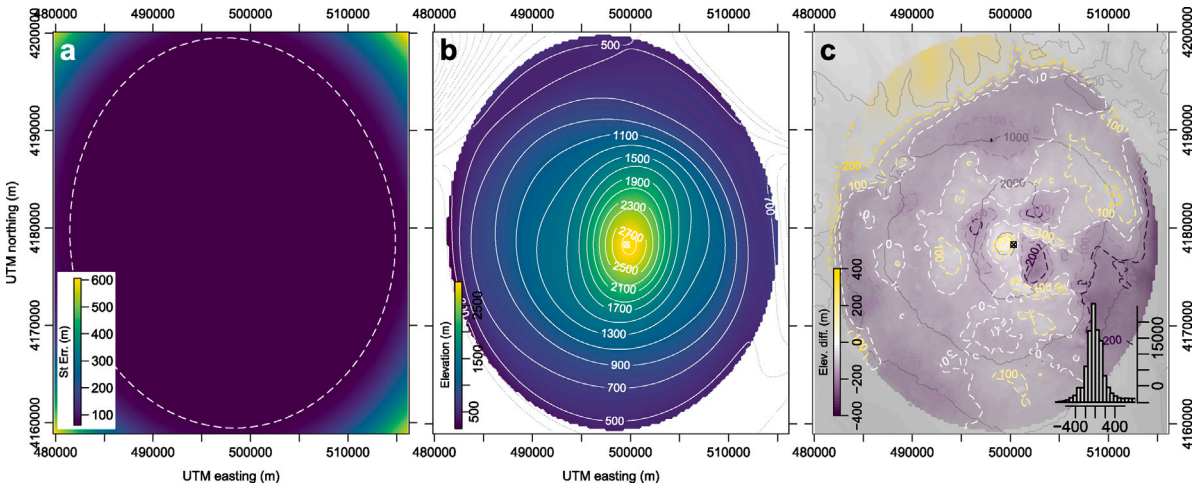

Fig. 3. (a) Standard error of the kriging interpolation of the fitted ellipses sampled at 20 m elevation intervals (Fig. 2a); the white dashed ellipse encloses the region with the lowest error. (b) Fitted reference surface resulting from ellipses interpolation shown inside the low-error region (white line in a); contour line interval is 200 m. (c) Map showing the difference between the observed elevation values (DEM) and the modelled fitted topography (residual topography); positive and negative residuals are represented in red and blue shades, respectively; the histogram shows the frequency distribution of the residual values.

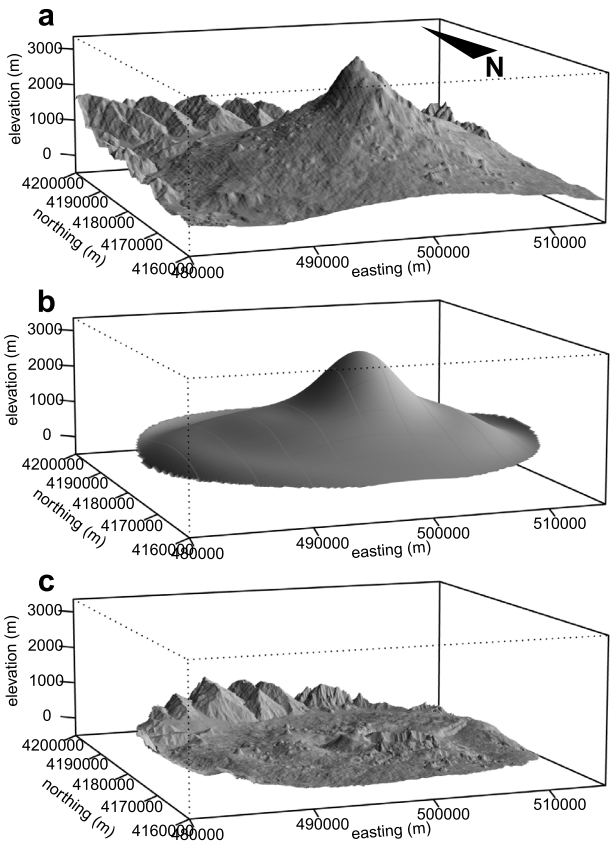

Fig. 4. 3d view of the morphology of Mt. Etna volcano (a), of the fitted reference surface (b), and of the residual topography (c).

Traces of the sections are drawn over the entire modelled surface area (Fig. 5a); however, the topographic profiles clearly indicate that the volcanic edifice extends only within a radial distance of approximately 15 km from the summit (Fig. 5b). In addition, at this distance, which corresponds to the average elevation of about 700 m a.s.l., the minimum value of eccentricity is recorded (Fig. 2c), indicating that the volcano approximates circular symmetry. This elevation can be considered a "base level", beyond which the effects of the surrounding terrains and the morphology of the basement becomes negligible. For this reason, all sections have been trimmed to a distance of ±15 km away from the center (Fig. 5c). The residuals series show a greater variability particularly in the sections of the eastern flank and at radial distance between about 2.5 and 6.0 from the center, corresponding to the zone with the maximum values of eccentricity (Fig. 2c).

Results of the wavelet analysis are shown in terms of peak values of the global wavelet power spectrum density for each single section. Specifically, for each section, the dominant wavelengths detected and their corresponding wavelet powers (i.e. the amplitude of each peak in the global WPS curves) are reported. The results are displayed by distinguishing between the primary dominant wavelength and any secondary one (Fig. 6a). The single wavelet power spectra, obtained by averaging each slope-parallel section, are also plotted (Fig. 6b). However, more interesting features emerge when grouping the curves according to their location on the volcano's flanks. The wavelength peaks are roughly aligned along two distinct bands: a shorter one at 6–8.5 km, and a longer one centered at about 10 km. These bands are not continuous in space; instead they alternate around the flank of the volcano. Based on the alignments recognized in Fig. 6a, the slope-parallel sections can be grouped into three distinct sectors, each exhibiting relatively homogeneous spectral characteristics and separated by marked transitions. Sectors are distinguished only on the base of similarity of spectral characteristics (i.e. wavelengths); therefore, in the same sector can fairly coexist topographic residuals of opposite sign or located at different positions along the flanks. In particular, group A (−12°−28°) is characterized by a dominant wavelength of about 6.5 km. Group B (28°−60°) is characterized by a dominant wavelength of about 10 km. Group C (60°−168°) shows a clear apparent spatial trend, with the main wavelength remaining almost constant at 6 km between 60° and 100°, then gradually increasing to 8.5 km at 140°. Finally, a few small clusters of localized, "anomalous" values can also be identified (blue diamonds in Fig. 6a). The Wavelet power spectrum for all 90 cross sections is shown in Figure S1. Their global wavelet power spectrum density, as well as for each of the three groups, is summarized in Fig. 6b, where vertical dashed lines indicate the peaks wavelengths of the curves.

All wavelet power spectra from sections within the same group (A to C) were stacked together to generate an average wavelet power spectrum representative of each sector. This procedure aims to enhance the most relevant features of each sector, to localize them in space, and highlighted possible radial symmetries (or asymmetries). The wavelet

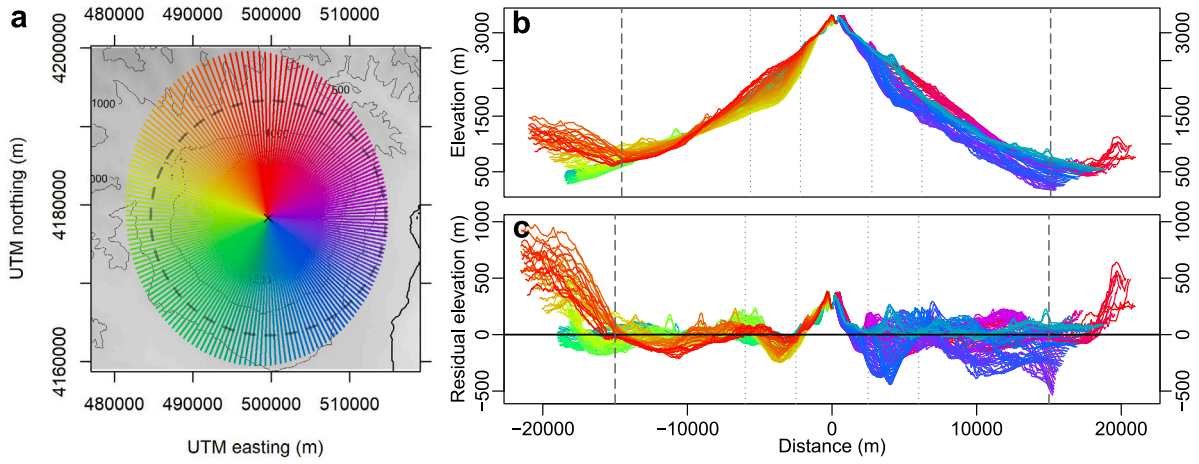

Fig. 5. (a) Map showing the traces of the 90, 2° spaced slope-parallel, sections; the origin of the lines is represented by the centre of the highest fitted ellipse at elevation of 3200 m. The dashed circle drawn at r = 15 km corresponds to the minimum of the circularity at elevation of about 700 m (see Fig. 2c) which encloses the portion of the volcanic edifice that can be considered as axisymmetric and excludes the surrounding non-volcanic terrains in the western and northern flanks. (b) Topographic slope-parallel sections and (c) topographic signals after the removal of the reference surface: the latter are used for the spectral analysis.

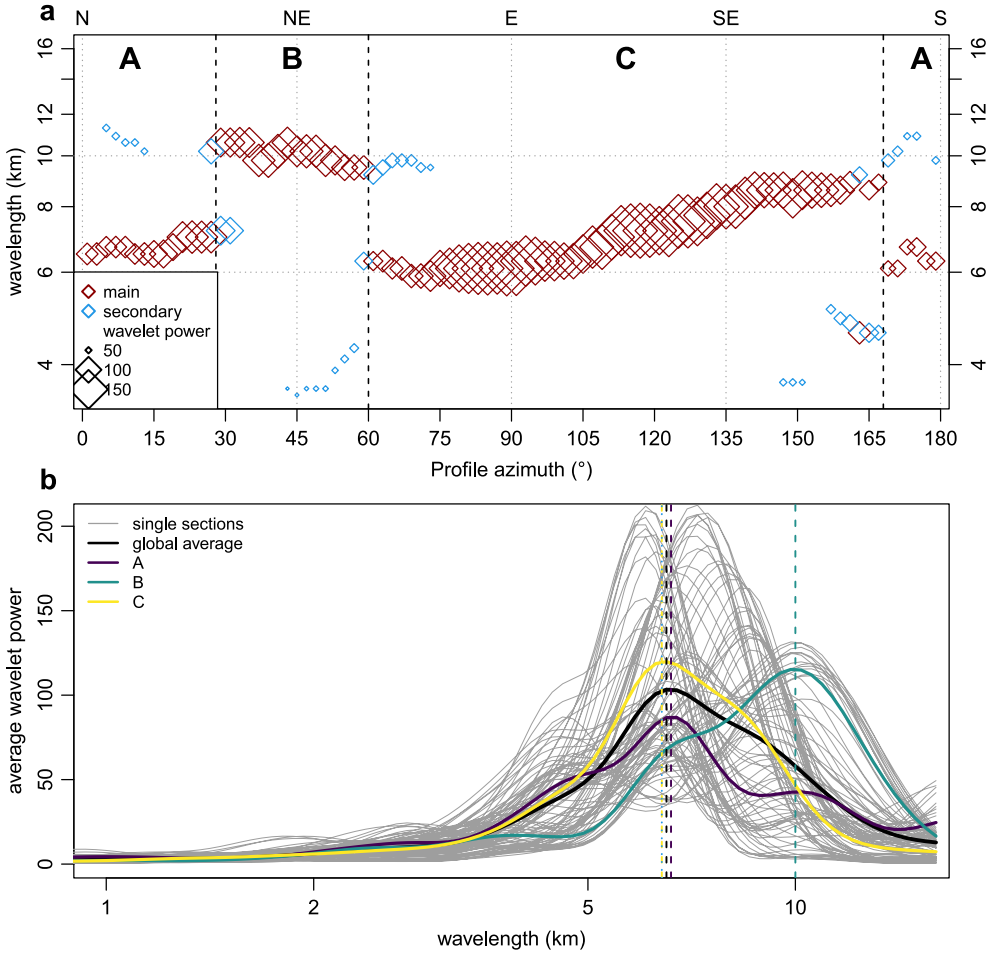

Fig. 6. (a) Results from wavelet analyses of residual topographic profiles in Fig. 5c. Red diamonds indicate the dominant wavelength values identified in each spectrum, the blue diamonds the secondary ones. The symbol size is proportional to the amplitude of each peak; circles indicate small groups of secondary wavelengths. Sections with similar characteristics have been grouped in three sectors labelled from "A" to "C"; see text for further explanations. (b) Global wavelet power spectrum density calculated for each of the 90 cross sections (grey curves) and averaged for radial sectors (coloured curves). Dashed lines indicate the primary peak for each sector, respectively. Data are summarized in Table 1.

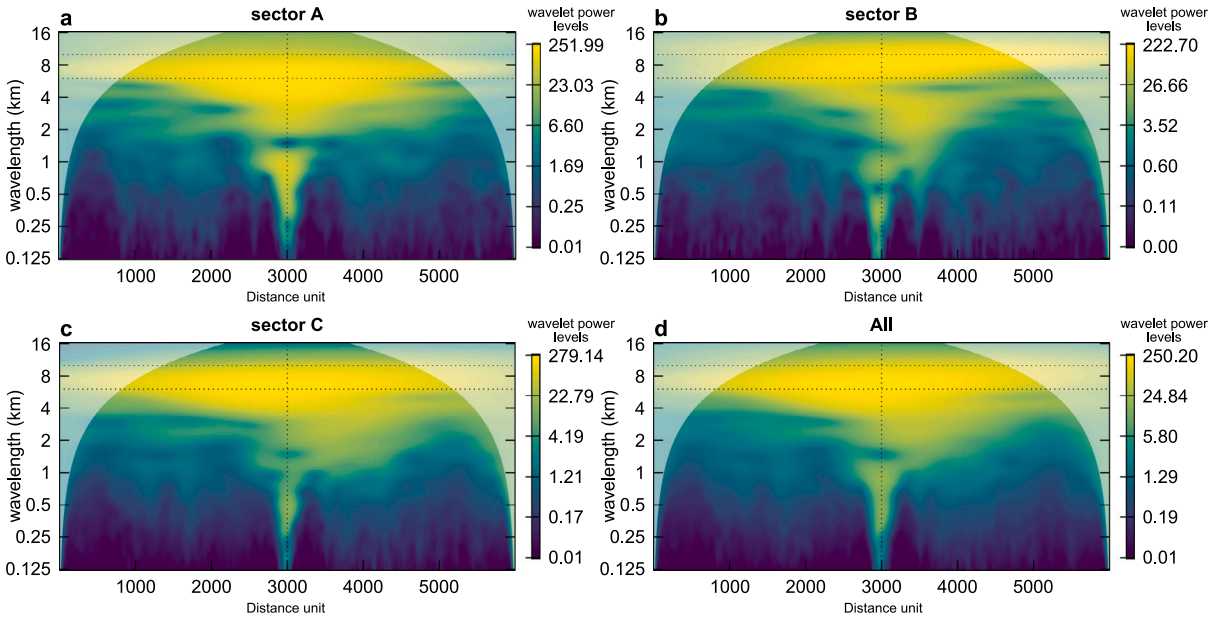

Fig. 7. (a):(c) Wavelet power spectrum of residual topographic slope-parallel sections stacked for geographic sectors (Fig. 6a). (d) Wavelet power spectrum averaged over the 90 cross sections. Distance unit = 5 m; horizontal lines provide reference at wavelength of 6, and 10 km (c.f. Fig. 6a) and the vertical dashed line indicates the centre of the volcanic edifice. Shaded regions in the upper corners represent the area of possible influence of edge effects.

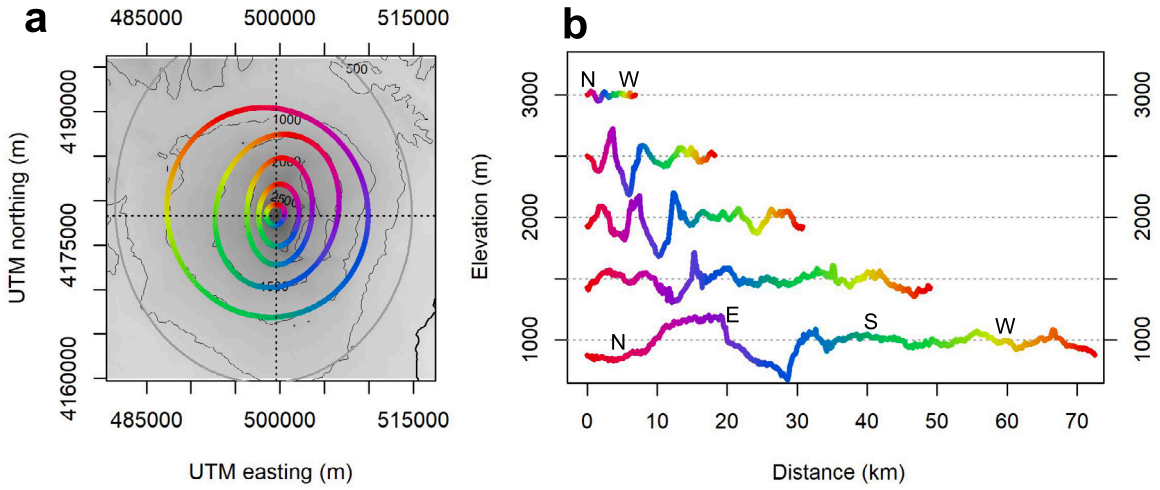

Fig. 8. (a) Map showing the traces of the base-parallel section drawn over the fitted ellipses at five different elevations. (b) Topographic signal used for the spectral analysis; the dashed horizontal lines provide references of the fitted topography (Fig. 4b).

power spectrum for sector A (Fig. 7a) is symmetric and reveals a region of high power centred along the volcano axis, marking wavelengths greater than 6 km. Additionally, the central region is characterized by high power values also at shorter wavelengths (≃1 km). In sector B, the region of highest wavelet power shifts towards longer wavelengths compared to sector A (Fig. 7b). The secondary wavelengths ($2 < km < 4$) recognized in Fig. 6a are localized on the right-hand side of the section (i.e. upper north-eastern flank of the volcano). In sector C, the area of higher wavelet power is centred and broadened over a wider range of wavelengths ($6 < km < 9$). Additionally, a region with relatively higher power, corresponding to the secondary wavelengths (Fig. 6a), shifts towards the right-hand side of the power spectrum, specifically aligning towards the south-eastern flank of the volcano.

Traces and elevation series of the five base-parallel sections are presented in Fig. 8. These sections are drawn at elevations ranging from 1000 to 3000 m a.s.l. at 500 m intervals. Except the inner ellipse, the topographic sections are characterized by marked variations localized in the eastern sector. In particular, some of these notable features can be recognized across the various traces, such as a bulge with NE orientation, and a topographic low that extends roughly across the SE wedge. The wavelet analysis was performed on the unwrapped traces of the ellipses, starting and ending at their northern tips.

The wavelet power spectra were computed individually for each base-parallel section. To minimize edge effects and preserve resolution at shorter wavelengths, each section was extended by adding a 2000 m segments at its both ends. The lengths of the sections vary from about 7 km to about 72 km. To enable their direct comparison, these sections were stretched along the distance axis to align their cardinal directions (Fig. 9, left column). The average power spectrum density plots showing the dominant wavelength are also presented (Fig. 9, right column).

Several prominent features are clearly recognizable in the power spectra. In particular, the three inner sections (between 3000 and 2000 m a.s.l.) show a peaked trend of the average power at 2, 4.8, and

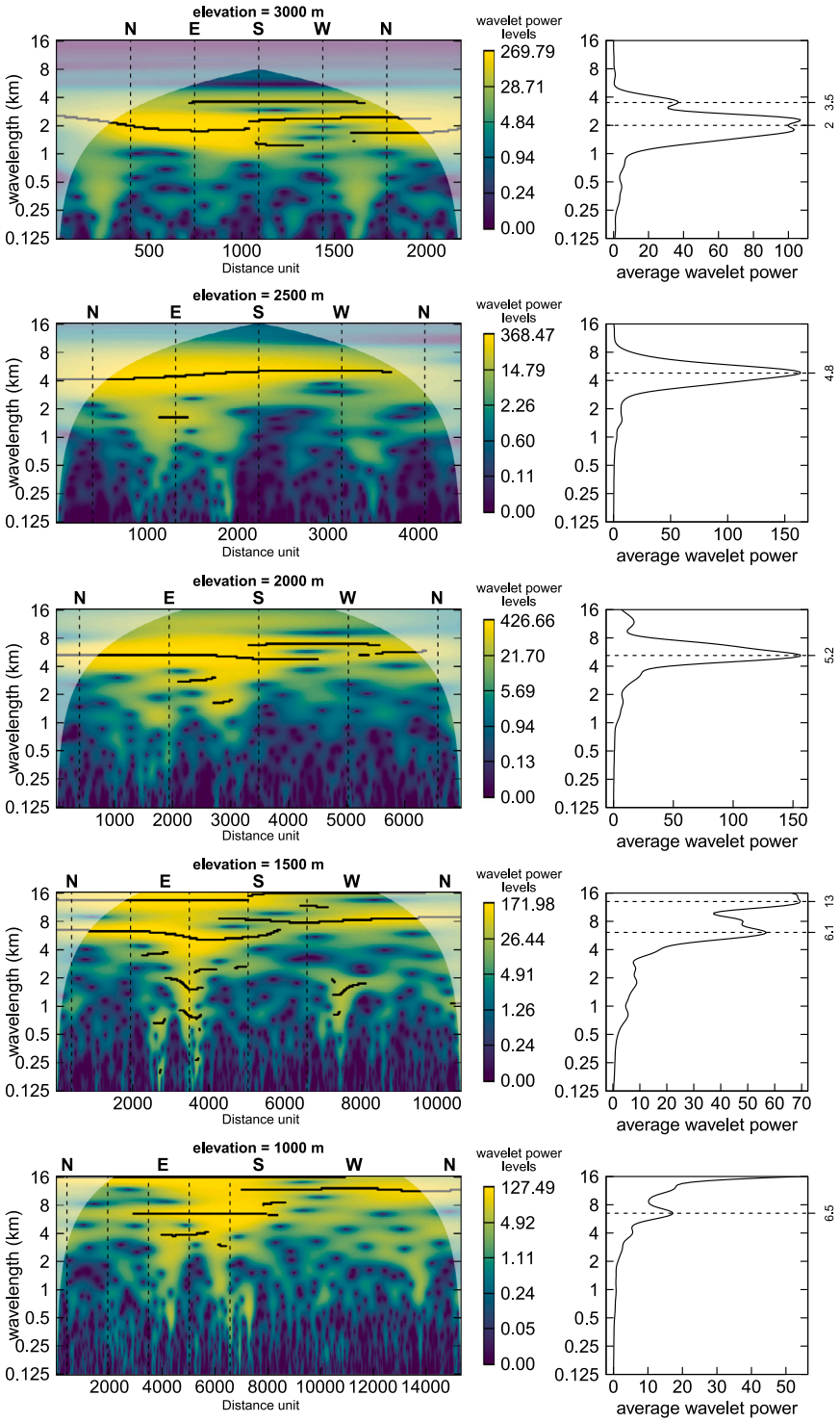

Fig. 9. Left column: wavelet power spectra of base-parallel topographic sections in Fig. 8b. Distance unit = 5 m; sections have been stretched to align them to geographical references (vertical dashed lines). Shaded regions in the upper corners represent the area of possible influence of edge effects and black contours indicate the significant period with 90% confidence level. Right column: averaged power spectrum densities of the base-parallel section; dashed lines indicate the main peaks; data are also summarized in Table 1.

5.2 km, with wavelet power corresponding to the main wavelengths being widespread along the entire length of the traces (i.e. around the flanks of the volcano). In the lower sections (1500 and 1000 m a.s.l.), the wavelet power is distributed over a larger bandwidth, with peaks emerging at 13 km and 6.1 km, and 6.5 km, respectively. In summary, wavelengths between 4.8 and 6.5 km characterize a significant portion of the volcanic edifice from 1000 to 2500 m a.s.l. At a smaller scale, shorter wavelength features (from ~ 4 down to ~ 1 km) emerge, affecting only limited portions of the sections; particularly in the eastern and southeastern sectors within the same elevation interval of 1000 – 2500

m a.s.l. (Fig. 9). To provide a comprehensive overview, the dominant wavelengths recognized in both slope- and base-parallel sections are reported in Table 1.

5. Discussion

The volcanic edifice of Mt. Etna, from approximately 700 m a.s.l. to the summit, can be well approximated by a surface described as the superposition of elliptical slices with nearly coaxial geometry. The goodness of the fitted surface is supported not only by the low errors associated to the ellipse fitting and interpolation, but also by the spectral analysis of the residual topography. The highest positive residuals are encountered in the outer north-western portion and they originate at the overlapping between the volcanic edifice and the Apenninic-Maghrebian Chain; for this reason this portion is out of the interest of this work and we focus into a circular region within 15 km away from the summit.

The presence of the first-order signal, characterized by its cusp shape (i.e. Etna's topographic profile, Fig. 4a), would have produced a distinctive wavelet power spectrum featuring a zone of high power in an axial position across all wavelengths, resulting in a distinct shape resembling an inverted cone. Such a feature is absent in the wavelet power spectra of the cross sections (Fig. 7a–e), allowing us to conclude that the first-order shape of the volcano has been accurately modelled and effectively filtered out.

The definition of a reference surface, and the subsequent application of wavelet decomposition, enabled the identification of topographic features characterized by different wavelengths, with particular emphasis on the main part of the volcanic edifice ($r \leq 15$ km). While the spectral features detected through the wavelet analysis can be reasonably interpreted in terms of source localization, the primary aim of this method is not the precise reconstruction and delineation of specific morphologies. Instead, it serves as a first-approximation for recognizing characteristic landforms and investigating their potential relationships with the geological, volcanological, and geomorphological processes (Doglioni and Simeone, 2014).

The wavelet decomposition of the cross sections reveals the occurrence of well-defined spectral features that appears as distinct bands (Fig. 6). These bands exhibit a degree of lateral continuity between adjacent sections, although occasional interruption occur. These breaks allowed the delineation of three sectors with distinct characteristics, separated by sharp transitions in wavelength. As expected, the three sectors identified through the wavelet analysis correspond with the map of the residual topography (Fig. 10a). Therefore, the features detected in both slope- and base-parallel sections are the spectral signatures of the residual, second-order topography.

In general, elements with shorter wavelet behaviour can be associated with localized topographic changes (e.g. ridges, valleys, rift zones), while those with longer wavelet behaviour correspond to large-scale morphological features, such as those involving broad portions of the volcano flank(s) or alignment extending across the entire volcano (Gomez, 2012). Some features that emerge following the removal of the first-order volcano shape (Fig. 10) were already sufficiently evident to be recognizable prior to filtering (Fig. 1b), whereas others became apparent only after topographical filtering.

At elevation below 1500 m a.s.l., the main wavelength is 6.5 km. In this outer part of the volcano, three topographic anomalies occur: two negative anomalies and positive one. A large negative anomaly marks the eastern flank of the volcano, an unstable and eastward sliding sector of Mt. Etna, which is the result of a combination of tectonic and volcanic processes and currently active (Bonforte et al., 2011; Palano, 2016; De Guidi et al., 2018; Palano et al., 2022, 2023). The exact timing of this sliding process is not fully constrained (Branca et al., 2014); however, this study suggests that its initiation occurred early enough to produce recognizable topographic effects or was sufficiently rapid to affect Holocene deposits. The negative anomaly on the northern flank and the positive anomaly on the north-eastern flank can be directly ascribable to the morphological bulge of the NE-Rift and to the Pernicana fault system, respectively. The latter system allows the sliding and lowering of the eastern flank. In this elevation interval, the eccentricity is low, indicating that the volcanic edifice tends to a circular symmetry. However, as elevation increases, the centre of symmetry shifts rapidly and systematically eastwards (Fig. 2b). This part of the volcanic edifice corresponds to the "Ellittico" volcano (60–15 ka), which encompassed the main construction phase of the current bulk of the Etna stratovolcano edifice (Branca et al., 2011a). During the activity of the "Ellittico", eruptive activity was primarily concentrated at the summit vents, with only secondary activity from flank fissures, accounting for the high degree of circular symmetry. Moreover, the shifting of the centres suggests that the feeding system migrated approximately 2 km eastwards before stabilizing near its present position.

At higher elevation, the belt from about 1500 to 2600 m a.s.l. is characterized by wavelet features of progressively decreasing wavelength (Table 1). Within this range, several positive and negative residuals occur (Fig. 10), with their positions and extents consistent with the dimensions of the wavelet features (Fig. 9). The negative anomaly on the eastern flank, coupled with two elongated positive anomalies, clearly correspond to the "Bove" valley depression and its relatively raised rims. The negative anomaly in the northeastern area marks a low sector bordered by active lineaments, mainly NE e ENE Rifts, where volcanic products of the "Ellittico" volcano (60–15 ka) are still exposed (Branca et al., 2011b). The two anomalies on the western flank, one positive and one negative, can be attributed to breaks of slope at the base of "Ellittico" stratovolcano. Interestingly, the three negative anomalies in this sector line up at 2400 m a.s.l. Within this elevation interval, the eccentricity of the fitted ellipses reaches its maximum values and ellipses are oriented along the N-S direction, consistent with the trajectory of their centres (Fig. 2b,c,d). This N-S elongation corresponds with the geometry of the two main volcanic rift zones active in the last 15 ka (NE and S Rifts), which are the sectors that have experienced recurrent dyke intrusions in the same elevation range (Branca et al., 2011a).

Finally, the positive anomaly centred at the summit of the volcano at elevations above 2800 m a.s.l., can be attributed to summit cone growth during the current phase of Etna's evolution (Mongibello volcano). This phase, followed the caldera-forming eruption that truncated the top of the "Ellittico" volcano, creating the "Ellittico" caldera at around 15 ka (Fig. 10b) (Coltelli et al., 2000; Branca et al., 2011b). This interpretation is supported by the centres of the fitted ellipses within this elevation interval (Fig. 2b), which correspond exactly to the present-day summit of the volcano.

Considering the radial coordinate (i.e. slope-parallel sections), the boundaries between the sectors, identified through wavelet analysis, correspond closely with the topographic anomalies, particularly the three larger anomalies located at lower elevations (Fig. 10a). Sector A is primarily characterized by relatively low topographic residuals and only includes two anomalies in its external portion due to the interaction between the lava flows and the underlying sedimentary basement. Sector B contains a major positive anomaly in the northeastern flank, which contributes to both the asymmetric wavelet power spectrum (Fig. 7b) and the longer average wavelength observed in this sector (Fig. 6). Sector C encompasses the "Bove" valley and the sliding flank, along with several smaller anomalies on the western side. The large, irregularly shaped negative anomaly in this sector may account for the apparent spatial trend of the wavelet features (Fig. 6). In all the three sectors, most topographic anomalies are located in the eastern half of the volcano, producing the asymmetric patterns observed in the wavelet power spectra of the slope-parallel sections and sectors (Fig. 7).

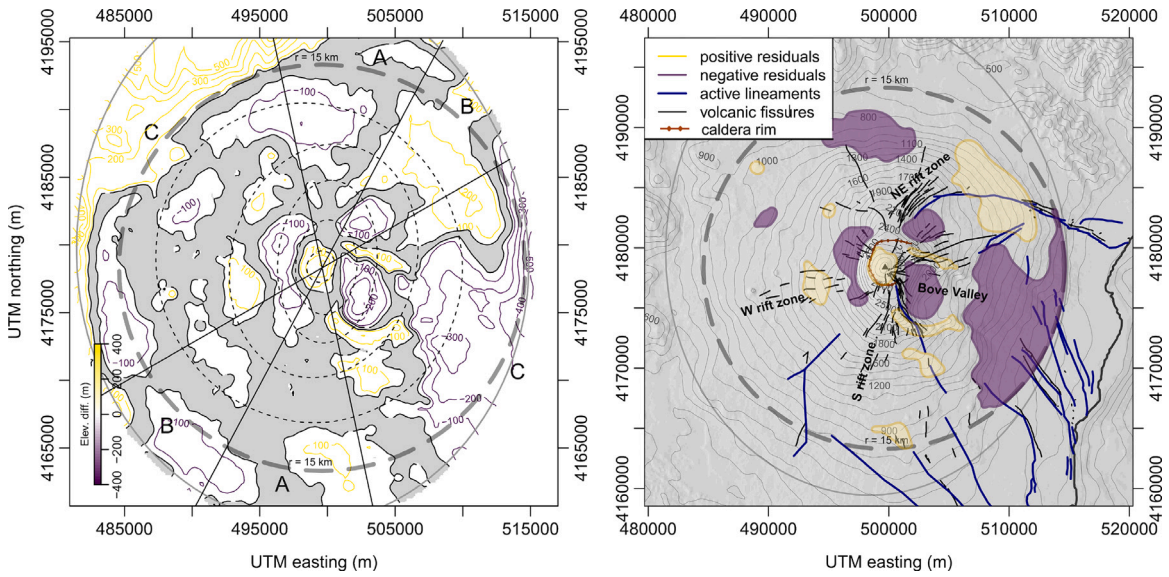

Fig. 10. (a) Schematic map of the residual topography showing the main positive and negative elements (yellow and purple contour lines, respectively), while the grey fill indicates the areas of low residual topography (< ±50 m). Dashed lines and ellipses provide references for sectors and base-parallel sections as discussed in the text. (b) Main features of (a) overlapped on Mt. Etna topography together with the main volcano-tectonic elements.

Table 1
List of the dominant wavelengths (in km) resulting from the wavelet analysis for the slope-parallel sectors and the base-parallel sections.

Sector	Main	Secondary
A	6.6	–
B	10	–
C	6.4	–
all	6.5	–
Ellipse elevation (m asl)	**Main**	**Secondary**
3000	2.0	3.5
2500	4.8	–
2000	5.2	–
1500	6.1	13
1000	6.5	–

6. Conclusions

This study presents a terrain analysis of Mt. Etna volcano using the wavelet decomposition method. The results are interpreted within the framework of the volcano's evolution and the volcano-tectonic currently shaping Mt. Etna. The main conclusions of this work may be summarized as follows:

- A reference surface, derived from the fitting of elliptical contours and their robust interpolation, effectively captures the first-order morphology of the volcanic edifice of Mt. Etna. After its removal, the resulting residual topography represents a valuable source of information, as it enhances the identification of second-order topographic features.
- The geometric parameters of the fitted ellipses, such as the eccentricity, center position, and rotation angle, can be correlated with the evolutionary stages of Mt. Etna, which contributed to the formation of the main volcanic edifices and that were distinguished on a stratigraphic base. In particular, it was possible to recognize a basal portion (below 1500 m a.s.l.) with circular symmetry and an eastwards-shifting axis; an intermediate portion distinctly elongated in the N-S direction; a terminal portion (above 2800 m a.s.l.) again showing circular symmetry, corresponding to the present summit. These three portions correspond to the active sliding flank on the shield volcano phase, to the "Ellittico" phase (60–15 ka), followed by the "Mongibello" phase that started after the collapse of the "Ellittico" summit area, and the formation of a caldera at 15 ka.
- The application of the wavelet decomposition reveals almost symmetric features at a broad scale. At finer scale, topographic features produce clear and distinct spectral signatures. By combining slope- and base-parallel sections, it is possible to recognize elements characterized by different wavelengths and to delineate sectors with different characteristics located on various parts of the volcano's flanks. The wavelength of wavelet features increases regularly moving from the summit outwards on the volcano flanks. Moreover, the wedge along the NE-SW direction has a distinct wavelength behaviour with respect the other sectors. Most of the features detected combining the topographic model and the wavelet analysis were correlated with previously known morphological, volcanic, and tectonic processes. Other identified may reflect the influence of buried morphological structures correlated to the same processes, although these relationships have not yet clearly established. As such, these "anomalous" regions represent important targets for future investigation.
- The proposed methodology can be exported to other case studies. The applicability is determined primarily by the characteristics of digital elevation models and the rate of volcanic resurface processes affecting the volcano flanks. Indeed, the availability of high-quality topographic data is expected to increase in the future thanks to advances in aerial or satellite platforms. A principal advantage of wavelet decomposition lies in its flexibility: following appropriate pre-processing, it can be easily tuned in terms of frequency bandwidth and spatial resolution to align with both the objectives of the investigation and the resolution of the available data.

CRediT authorship contribution statement

Salvatore Scudero: Writing – review & editing, Writing – original draft, Validation, Methodology, Investigation, Formal analysis, Data curation, Conceptualization. **Gianluca Groppelli:** Writing – review & editing, Validation.

Fundings

This research did not receive any specific grant from funding agencies in the public, commercial, or not-for-profit sectors.

Declaration of competing interest

The authors declare that they have no known competing financial interests or personal relationships that could have appeared to influence the work reported in this paper.

Acknowledgement

The authors thank Emanuela Di Martino (University of Catania) for her careful review of the early version of the manuscript. The authors also thank Emanuela De Beni and an anonymous reviewer for their useful comments on the early version of the manuscript, and Lucia Capra Editor of Journal of Volcanology and Geothermal Research.

Appendix A. Supplementary data

Supplementary material related to this article can be found online at https://doi.org/10.1016/j.jvolgeores.2025.108443.

Data availability

The data used for this research are derived from Regione Siciliana (2013).

References

Barreca, G., Bonforte, A., Neri, M., 2013. A pilot GIS database of active faults of Mt. Etna (Sicily): A tool for integrated hazard evaluation. J. Volcanol. Geotherm. Res. 251, 170–186.
Barreca, G., Branca, S., Corsaro, R.A., Scarfì, L., Cannavò, F., Aloisi, M., Monaco, C., Faccenna, C., 2020. Slab detachment, mantle flow, and crustal collision in eastern Sicily (southern Italy): Implications on Mount Etna volcanism. Tectonics 39 (9), e2020TC006188.
Barreca, G., Branca, S., Monaco, C., 2018a. Three-dimensional modeling of Mount Etna volcano: Volume assessment, trend of eruption rates, and geodynamic significance. Tectonics 37 (3), 842–857.
Barreca, G., Corradino, M., Monaco, C., Pepe, F., 2018b. Active tectonics along the south east offshore margin of Mt. Etna: New insights from high-resolution seismic profiles. Geosciences 8 (2), 62.
Bonforte, A., Guglielmino, F., Coltelli, M., Ferretti, A., Puglisi, G., 2011. Structural assessment of Mount Etna volcano from permanent scatterers analysis. Geochem. Geophys. Geosystems 12 (2).
Bossis, R., Regard, V., Carretier, S., 2023. Initial shape reconstruction of a volcanic island as a tool for quantifying long-term coastal erosion: the case of Corvo Island (Azores). Earth Surf. Dyn. 11 (3), 529–545.
Branca, S., Coltelli, M., De Beni, E., Wijbrans, J., 2008. Geological evolution of Mount Etna volcano (Italy) from earliest products until the first central volcanism (between 500 and 100 ka ago) inferred from geochronological and stratigraphic data. Int. J. Earth Sci. 97, 135–152.
Branca, S., Coltelli, M., Groppelli, G., 2011a. Geological evolution of a complex basaltic stratovolcano: Mount Etna, Italy. Ital. J. Geosci. 130 (3), 306–317.
Branca, S., Coltelli, M., Groppelli, G., Lentini, F., 2011b. Geological map of Etna volcano, 1: 50,000 scale. Ital. J. Geosci. 130 (3), 265–291.
Branca, S., De Guidi, G., Lanzafame, G., Monaco, C., 2014. Holocene vertical deformation along the coastal sector of Mt. Etna volcano (eastern Sicily, Italy): implications on the time–space constrains of the volcano lateral sliding. J. Geodyn. 82, 194–203.
Branca, S., Ferrara, V., 2013. The morphostructural setting of Mount Etna sedimentary basement (Italy): Implications for the geometry and volume of the volcano and its flank instability. Tectonophysics 586, 46–64.
Cadio, C., Ballmer, M.D., Panet, I., Diament, M., Ribe, N., 2012. New constraints on the origin of the hawaiian swell from wavelet analysis of the geoid to topography ratio. Earth Planet. Sci. Lett. 359, 40–54.
Calvari, S., Tanner, L.H., Groppelli, G., 1998. Debris-avalanche deposits of the Milo Lahar sequence and the opening of the Valle del Bove on Etna volcano (Italy). J. Volcanol. Geotherm. Res. 87 (1–4), 193–209.
Calvari, S., Tanner, L.H., Groppelli, G., Norini, G., 2004. Valle del Bove, eastern flank of Etna volcano: a comprehensive model for the opening of the depression and implications for future hazards. In: Etna Volcano Laboratory. American Geophysical Union.
Carrión-Mero, P., Montalván-Burbano, N., Paz-Salas, N., Morante-Carballo, F., 2020. Volcanic geomorphology: a review of worldwide research. Geosciences 10 (9), 347.
Catalano, S., De Guidi, G., Monaco, C., Tortorici, G., Tortorici, L., 2008. Active faulting and seismicity along the Siculo–Calabrian Rift Zone (Southern Italy). Tectonophysics 453 (1–4), 177–192.
Chamoli, A., 2009. Wavelet analysis of geophysical time series. Earth Sci. India 2.
Chernov, N., Huang, Q., Ma, H., 2014. Fitting quadratic curves to data points. Br. J. Math. Comput. Sci. 4 (1), 33–60.
Coltelli, M., Del Carlo, P., Vezzoli, L., 2000. Stratigraphic constraints for explosive activity in the past 100 ka at Etna volcano, Italy. Int. J. Earth Sci. 89, 665–677.
Cosburn, K., Roy, M., 2020. Analysing the topographic form of stratovolcanoes. J. Volcanol. Geotherm. Res. 407, 107123.
Daubechies, I., 1992. Ten Lectures on Wavelets, vol. 61, Siam.
Davidson, J., De Silva, S., et al., 2000. Composite volcanoes. Encycl. Volcanoes 1, 663–681.
De Beni, E., Branca, S., Coltelli, M., Groppelli, G., Wijbrans, J.R., 2011. 40Ar/39Ar isotopic dating of Etna volcanic succession. Ital. J. Geosci. 130 (3), 292–305.
De Beni, E., Proietti, C., Cantarero, M., Greco, F., Mirabella, L.T., Messina, A.A., Carbone, D., Papčo, J., Zahorec, P., Vajda, P., 2025. The dynamic summer of 2024 at Etna volcano documented by UAS: morphological changes and their gravimetric effects. In: IAVCEI Meeting, Geneva, 29th June - 4th July 2025. p. 2425.
De Guidi, G., Brighenti, F., Carnemolla, F., Imposa, S., Marchese, S.A., Palano, M., Scudero, S., Vecchio, A., 2018. The unstable eastern flank of Mt. Etna volcano (Italy): First results of a GNSS-based network at its southeastern edge. J. Volcanol. Geotherm. Res. 357, 418–424.
De Guidi, G., Caputo, R., Scudero, S., 2013. Regional and local stress field orientation inferred from quantitative analyses of extension joints: case study from southern Italy. Tectonics 32 (2), 239–251.
De Guidi, G., Imposa, S., Scudero, S., Palano, M., 2014. New evidence for late quaternary deformation of the substratum of Mt. Etna volcano (Sicily, Italy): clues indicate active crustal doming. Bull. Volcanol. 76, 1–13.
De Guidi, G., Scudero, S., Gresta, S., 2012. New insights into the local crust structure of Mt. Etna volcano from seismological and morphotectonic data. J. Volcanol. Geotherm. Res. 223, 83–92.
de Silva, S., Lindsay, J.M., 2015. Primary volcanic landforms. In: The Encyclopedia of Volcanoes. Elsevier, pp. 273–297.
Del Ben, A., Barnaba, C., Taboga, A., 2008. Strike-slip systems as the main tectonic features in the plio-quaternary kinematics of the Calabrian Arc. Mar. Geophys. Res. 29 (1), 1–12.
Di Stefano, A., Branca, S., 2002. Long-term uplift rate of the Etna volcano basement (southern Italy) based on biochronological data from pleistocene sediments. Terra Nova 14 (1), 61–68.
Dibacto, S., Lahitte, P., Karátson, D., Hencz, M., Szakács, A., Biró, T., Kovács, I., Veres, D., 2020. Growth and erosion rates of the east carpathians volcanoes constrained by numerical models: Tectonic and climatic implications. Geomorphology 368, 107352.
Doglioni, C., Innocenti, F., Mariotti, G., 2001. Why Mt Etna? Terra Nova 13 (1), 25–31.
Doglioni, A., Simeone, V., 2014. Geomorphometric analysis based on discrete wavelet transform. Environ. Earth Sci. 71, 3095–3108.
Faccenna, C., Molin, P., Orecchio, B., Olivetti, V., Bellier, O., Funiciello, F., Minelli, L., Piromallo, C., Billi, A., 2011. Topography of the Calabria subduction zone (southern Italy): Clues for the origin of Mt. Etna. Tectonics 30 (1).
Favalli, M., Fornaciai, A., Nannipieri, L., Harris, A., Calvari, S., Lormand, C., 2018. UAV-based remote sensing surveys of lava flow fields: a case study from Etna's 1974 channel-fed lava flows. Bull. Volcanol. 80, 1–18.
Favalli, M., Innocenti, F., Pareschi, M.T., Pasquarè, G., Mazzarini, F., Branca, S., Cavarra, L., Tibaldi, A., 1999. The DEM of Mt. Etna: geomorphological and structural implications. Geodin. Acta 12 (5), 279–290.
Favalli, M., Karátson, D., Mazzarini, F., Pareschi, M.T., Boschi, E., 2009. Morphometry of scoria cones located on a volcano flank: a case study from Mt. Etna (Italy), based on high-resolution LiDAR data. J. Volcanol. Geotherm. Res. 186 (3–4), 320–330.
Favalli, M., Karátson, D., Mazzuoli, R., Pareschi, M.T., Ventura, G., 2005. Volcanic geomorphology and tectonics of the Aeolian archipelago (southern Italy) based on integrated DEM data. Bull. Volcanol. 68, 157–170.
Favalli, M., Karátson, D., Yepes, J., Nannipieri, L., 2014. Surface fitting in geomorphology—Examples for regular-shaped volcanic landforms. Geomorphology 221, 139–149.
Firetto Carlino, M., Cavallaro, D., Coltelli, M., Cocchi, L., Zgur, F., Patanè, D., 2019. Time and space scattered volcanism of Mt. Etna driven by strike-slip tectonics. Sci. Rep. 9 (1), 1–15.
Franklin, S.E., 2020. Interpretation and use of geomorphometry in remote sensing: a guide and review of integrated applications. Int. J. Remote Sens. 41 (19), 7700–7733.
Gambino, S., Barreca, G., Bruno, V., De Guidi, G., Ferlito, C., Gross, F., Mattia, M., Scarfì, L., Monaco, C., 2022. Transtension at the northern termination of the Alfeo-Etna fault system (western ionian sea, Italy): Seismotectonic implications and relation with Mt. Etna volcanism. Geosciences 12 (3), 128.
Gayer, E., Michon, L., Villeneuve, N., 2021. Volcanic island multi-stage construction inferred from a simple geometrical approach: Example of Réunion island. Geomorphology 392, 107900.
Gomez, C., 2012. Multi-scale topographic analysis of Merbabu and Merapi volcanoes using wavelet decomposition. Environ. Earth Sci. 67, 1423–1430.

Gomez, C., 2018. Understanding volcanic geomorphology from derivatives and wavelet analysis: A case study at Miyakejima volcano, Izu islands, Japan. J. Volcanol. Geotherm. Res. 354, 57–66.
Gomez, C., 2022. Pointcloud and volcanic geomorphology. In: Point Cloud Technologies for Geomorphologists: From Data Acquisition To Processing. Springer, pp. 103–120.
Grosse, P., De Vries, B.V.W., Euillades, P.A., Kervyn, M., Petrinovic, I.A., 2012. Systematic morphometric characterization of volcanic edifices using digital elevation models. Geomorphology 136 (1), 114–131.
Grosse, P., Euillades, P.A., Euillades, L.D., Van Wyk de Vries, B., 2014. A global database of composite volcano morphometry. Bull. Volcanol. 76, 1–16.
Grosse, P., Kervyn, M., 2018. Morphometry of terrestrial shield volcanoes. Geomorphology 304, 1–14.
Grosse, P., van Wyk de Vries, B., Petrinovic, I.A., Euillades, P.A., Alvarado, G.E., 2009. Morphometry and evolution of arc volcanoes. Geology 37 (7), 651–654.
Grossmann, A., Morlet, J., 1984. Decomposition of Hardy functions into square integrable wavelets of constant shape. SIAM J. Math. Anal. 15 (4), 723–736.
Guest, J., Chester, D., Duncan, A., 1984. The Valle del Bove, Mount Etna: its origin and relation to the stratigraphy and structure of the volcano. J. Volcanol. Geotherm. Res. 21 (1–2), 1–23.
Guillou-Frottier, L., Burov, E., Nehlig, P., Wyns, R., 2007. Deciphering plume–lithosphere interactions beneath Europe from topographic signatures. Glob. Planet. Change 58 (1–4), 119–140.
Gvirtzman, Z., Nur, A., 1999. The formation of Mount Etna as the consequence of slab rollback. Nature 401 (6755), 782–785.
Jordan, G., Schott, B., 2005. Application of wavelet analysis to the study of spatial pattern of morphotectonic lineaments in digital terrain models. A case study. Remote Sens. Environ. 94 (1), 31–38.
Kalbermatten, M., Van De Ville, D., Turberg, P., Tuia, D., Joost, S., 2012. Multiscale analysis of geomorphological and geological features in high resolution digital elevation models using the wavelet transform. Geomorphology 138 (1), 352–363.
Karátson, D., Favalli, M., Tarquini, S., Fornaciai, A., Wörner, G., 2010a. The regular shape of stratovolcanoes: a DEM-based morphometrical approach. J. Volcanol. Geotherm. Res. 193 (3–4), 171–181.
Karátson, D., Telbisz, T., Singer, B.S., 2010b. Late-stage volcano geomorphic evolution of the Pleistocene San Francisco Mountain, Arizona (USA), based on high-resolution DEM analysis and 40 Ar/39 Ar chronology. Bull. Volcanol. 72, 833–846.
Karátson, D., Telbisz, T., Woerner, G., 2012. Erosion rates and erosion patterns of Neogene to Quaternary stratovolcanoes in the Western Cordillera of the Central Andes: an SRTM DEM based analysis. Geomorphology 139, 122–135.
Karátson, D., Yepes, J., Favalli, M., Rodríguez-Peces, M.J., Fornaciai, A., 2016. Reconstructing eroded paleovolcanoes on Gran Canaria, Canary Islands, using advanced geomorphometry. Geomorphology 253, 123–134.
Karlstrom, L., Richardson, P.W., O'Hara, D., Ebmeier, S.K., 2018. Magmatic landscape construction. J. Geophys. Res.: Earth Surf. 123 (8), 1710–1730.
Kereszturi, G., Geyer, A., Martí, J., Németh, K., Dóniz-Páez, F.J., 2013. Evaluation of morphometry-based dating of monogenetic volcanoes—a case study from Bandas del Sur, Tenerife (Canary islands). Bull. Volcanol. 75, 1–19.
Lahitte, P., Samper, A., Quidelleur, X., 2012. DEM-based reconstruction of southern Basse-Terre volcanoes (Guadeloupe archipelago, FWI): Contribution to the Lesser Antilles Arc construction rates and magma production. Geomorphology 136 (1), 148–164.
Lashermes, B., Foufoula-Georgiou, E., Dietrich, W.E., 2007. Channel network extraction from high resolution topography using wavelets. Geophys. Res. Lett. 34 (23).
Lescinsky, D.T., Skoblenick, S.V., Mansinha, L., 2007. Automated identification of lava flow structures using local Fourier spectrum of digital elevation data. J. Geophys. Res.: Solid Earth 112 (B5).
Little, S.A., Carter, P.H., Smith, D.K., 1993. Wavelet analysis of a bathymetric profile reveals anomalous crust. Geophys. Res. Lett. 20 (18), 1915–1918.
Malaguti, A.B., Branca, S., Speranza, F., Coltelli, M., Del Carlo, P., Renzulli, A., 2023. Age of the Valle del Bove formation and chronology of the post-collapse flank eruptions, Etna volcano (Italy). J. Volcanol. Geotherm. Res. 434, 107752.
Maxwell, A.E., Shobe, C.M., 2022. Land-surface parameters for spatial predictive mapping and modeling. Earth-Sci. Rev. 226, 103944.
Monaco, C., Tapponnier, P., Tortorici, L., Gillot, P., 1997. Late quaternary slip rates on the acireale-piedimonte normal faults and tectonic origin of Mt. Etna (Sicily). Earth Planet. Sci. Lett. 147 (1–4), 125–139.
Norini, G., Groppelli, G., Capra, L., De Beni, E., 2004. Morphological analysis of Nevado de Toluca volcano (Mexico): new insights into the structure and evolution of an andesitic to dacitic stratovolcano. Geomorphology 62 (1–2), 47–61.
O'Hara, D., Goren, L., Van Wees, R.M., Campforts, B., Grosse, P., Lahitte, P., Kereszturi, G., Kervyn, M., 2024. Time-varying drainage basin development and erosion on volcanic edifices. Earth Surf. Dyn. 12 (3), 709–726.
O'Hara, D., Karlstrom, L., 2023. The arc-scale spatial distribution of volcano erosion implies coupled magmatism and regional climate in the Cascades arc, United States. Front. Earth Sci. 11, 1150760.
Palano, M., 2016. Episodic slow slip events and seaward flank motion at Mt. Etna volcano (Italy). J. Volcanol. Geotherm. Res. 324, 8–14.
Palano, M., Calcaterra, S., Gambino, P., Porfidia, B., Sparacino, F., 2023. GNSS-based long-term deformation at Mount Etna volcano (Italy). Results Geophys. Sci. 14, 100056.
Palano, M., Sparacino, F., Gambino, P., D'Agostino, N., Calcaterra, S., 2022. Slow slip events and flank instability at Mt. Etna volcano (Italy). Tectonophysics 836, 229414.
Perron, J.T., Kirchner, J.W., Dietrich, W.E., 2008. Spectral signatures of characteristic spatial scales and nonfractal structure in landscapes. J. Geophys. Res.: Earth Surf. 113 (F4).
Polonia, A., Torelli, L., Mussoni, P., Gasperini, L., Artoni, A., Klaeschen, D., 2011. The Calabrian Arc subduction complex in the ionian sea: Regional architecture, active deformation, and seismic hazard. Tectonics 30 (5).
R Development Core Team, 2005. R: A Language and Environment for Statistical Computing. R Foundation for Statistical Computing, Vienna, Austria, ISBN: 3-900051-07-0.
Regione Siciliana, 2013. Modello digitale del terreno (MDT) 2 m x 2 m regione siciliana-ATA 2012–2013. Dataset.
Ricci, J., Quidelleur, X., Lahitte, P., 2015. Volcanic evolution of central Basse-Terre island revisited on the basis of new geochronology and geomorphology data. Bull. Volcanol. 77, 1–17.
Roesch, A., Schmidbauer, H., Roesch, M.A., 2014. Package 'WaveletComp'.
Salvany, T., Lahitte, P., Nativel, P., Gillot, P.-Y., 2012. Geomorphic evolution of the Piton des Neiges volcano (Réunion Island, Indian Ocean): competition between volcanic construction and erosion since 1.4 Ma. Geomorphology 136 (1), 132–147.
Schellart, W., 2010. Mount Etna–Iblean volcanism caused by rollback-induced upper mantle upwelling around the ionian slab edge: an alternative to the plume model. Geology 38 (8), 691–694.
Scudero, S., 2024. Crustal stress pattern at Mt. Etna volcano. J. Geodyn. 102017.
Scudero, S., De Guidi, G., Gudmundsson, A., 2019. Size distributions of fractures, dykes, and eruptions on Etna, Italy: Implications for magma-chamber volume and eruption potential. Sci. Rep. 9 (1), 1–9.
Scudero, S., De Guidi, G., Imposa, S., Currenti, G., 2015. Modelling the long-term deformation of the sedimentary substrate of Mt. Etna volcano (Italy). Terra Nova 27 (5), 338–345.
Struble, W.T., Roering, J.J., 2021. Hilltop curvature as a proxy for erosion rate: wavelets enable rapid computation and reveal systematic underestimation. Earth Surf. Dyn. 9 (5), 1279–1300.
Struble, W.T., Roering, J.J., Dorsey, R.J., Bendick, R., 2021. Characteristic scales of drainage reorganization in Cascadia. Geophys. Res. Lett. 48 (3), e2020GL091413.
Székely, B., Karátson, D., 2004. DEM-based morphometry as a tool for reconstructing primary volcanic landforms: examples from the Börzsöny mountains, Hungary. Geomorphology 63 (1–2), 25–37.
Tarquini, S., Favalli, M., Mazzarini, F., Isola, I., Fornaciai, A., 2012. Morphometric analysis of lava flow units: case study over LIDAR-derived topography at Mount Etna, Italy. J. Volcanol. Geotherm. Res. 235, 11–22.
Thouret, J.-C., 1999. Volcanic geomorphology—an overview. Earth-Sci. Rev. 47 (1–2), 95–131.
Tort, A., Finizola, A., 2005. The buried caldera of Misti volcano, Peru, revealed by combining a self-potential survey with elliptic Fourier function analysis of topography. J. Volcanol. Geotherm. Res. 141 (3–4), 283–297.
Urlaub, M., Petersen, F., Gross, F., Bonforte, A., Puglisi, G., Guglielmino, F., Krastel, S., Lange, D., Kopp, H., 2018. Gravitational collapse of Mount Etna's southeastern flank. Sci. Adv. 4 (10), eaat9700.
Wilson, J.P., 2022. Recent Advances and Challenges in Geomorphometry. Elsevier.
Xiong, L., Li, S., Tang, G., Strobl, J., 2022. Geomorphometry and terrain analysis: Data, methods, platforms and applications. Earth-Sci. Rev. 104191.
Xu, Y., Zhang, S., Li, J., Liu, H., Zhu, H., 2021. Extracting terrain texture features for landform classification using wavelet decomposition. ISPRS Int. J. Geo-Information 10 (10), 658.
Zarazúa-Carbajal, M.C., De la Cruz-Reyna, S., 2020. Morpho-chronology of monogenetic scoria cones from their level contour curves. Applications to the Chichinautzin monogenetic field, Central Mexico. J. Volc. Geoth. Res. 407, 107093.